



41st European Rotorcraft Forum
Munich, 1-4 September, 2015
Paper 42

NUMERICAL SIMULATION OF THE ERICA TILTROTOR USING THE HMB2 SOLVER

Antonio Jimenez Garcia
antjim@liverpool.ac.uk
PhD student

CFD Laboratory, School of Engineering
University of Liverpool, United Kingdom

George N. Barakos
G.Barakos@liverpool.ac.uk
Professor

CFD Laboratory, School of Engineering
University of Liverpool, United Kingdom

Abstract

Numerical simulations of the Enhanced Rotorcraft Innovative Concept Achievement tiltrotor have been performed using the Helicopter Multi-Block CFD solver. Comparisons with experimental data obtained in the German-Dutch Large Low-speed Facility and the S1MA wind tunnel are also presented. For this work, an aeroplane mode configuration, referred to as AC1, of the tiltrotor is considered. It is characterised by low speed and relatively high angle of attack of the aircraft. The Helicopter Multi-Block CFD method predicted the surface pressure coefficient at cross sections on the fuselage, nacelle, fixed wing, and tiltable wing of the tiltrotor accurately. Good overall agreement is obtained between CFD and wind tunnel data. In addition to fully resolved blades, computations with actuator disk models were also performed.

1 INTRODUCTION

To address the lack of knowledge and experience with tiltrotors, the European Commission funded the NICETRIP [1] project (Novel Innovative Competitive Effective Tilt Rotor Integrated Project). Within this project, 1:8 non motorised and 1:5 motorised scale-model tiltrotors were designed and manufactured under the name of ERICA (Enhanced Rotorcraft Innovative Concept Achievement).

For the 1:5 motorised scale-model tiltrotor, the experiments were carried out in the 9.5x9.5m DNW-LLF (German-Dutch Wind Tunnels Large Low-speed Facility) and the 8m S1MA ONERA (Of-

fice National d'Etudes et de Recherches Aeronautiques) wind tunnels. Conversion corridor configurations were studied in the subsonic 9.5x9.5m wind tunnel in the DNW-LLF [2]. The test programme covered the low speed range (freestream Mach numbers 0 to 0.168) of the flight envelope from helicopter mode, where the nacelles were tilted 90 degrees relative to the aircraft, to aeroplane mode. The model was supported via a ventral sting. The high speed test campaign (from freestream Mach number 0.168 to 0.55) was conducted in the test section no.2 of the ONERA [3]. The S1MA was equipped with a straight sting located at the rear

Copyright Statement© The authors confirm that they, and/or their company or organisation, hold copyright on all of the original material included in this paper. The authors also confirm that they have obtained permission, from the copyright holder of any third party material included in this paper, to publish it as part of their paper. The authors confirm that they give permission, or have obtained permission from the copyright holder of this paper, for the publication and distribution of this paper as part of the ERF2015 proceedings or as individual offprints from the proceedings and for inclusion in a freely accessible web-based repository.

part of the fuselage. The aim of this test was to study the aerodynamic interactions between different components of the ERICA tiltrotor at high velocity.

During experiments, the following measurements were performed: forces and moments acting on the model by means of a 6-component main balance, unsteady pressure distribution measured by means of Kulite sensors, and steady pressure distribution by means of static pressure taps.

This paper shows the aerodynamic characterisation of the 1:5 motorised scale-model of the ERICA tiltrotor. The experimental data is used here to validate the HMB2 (Helicopter Multi-Block) CFD method developed at the University of Liverpool [4, 5, 6, 7].

2 HMB2 CFD SOLVER

The HMB2 [4, 5, 6, 7] code, developed at Liverpool, is used as the CFD solver for the present work. It solves the Navier-Stokes equations in integral form using the arbitrary Lagrangian Eulerian (ALE) formulation, first proposed by Hirt et al. [8], for time-dependent domains, which may include moving boundaries. The Navier-Stokes equations are discretised using a cell-centred finite volume approach on a multi-block grid. The spatial discretisation of these equations leads to a set of ordinary differential equations in time,

$$(1) \quad \frac{d}{dt}(\mathbf{w}_{i,j,k} V_{i,j,k}) = -\mathbf{R}_{i,j,k}(\mathbf{w})$$

where i, j, k represent the cell index, \mathbf{w} and \mathbf{R} are the vector of conservative variables and flux residual, respectively, and $V_{i,j,k}$ is the volume of the cell i, j, k . Osher's [9] upwind scheme is used to discretise the convective terms in space, whereas viscous terms are discretised using second order central differencing. The Monotone Upstream-centred Schemes for Conservation Laws (MUSCL) developed by van Leer [10] is used to provide third order accuracy in space. The HMB2 solver uses the alternative form of the van Albada limiter [11] being activated in regions where a large gradients are encountered mainly due to shock waves, avoiding the non-physical spurious oscillations. An implicit dual-time stepping method is employed to performed the temporal integration, and the solution is marching in pseudo-time iterations to achieve fast convergence. The linearised system of equations

is solved using the Generalised Conjugate Gradient method with a Block Incomplete Lower-Upper (BILU) factorisation as a pre-conditioner [12]. Because implicit scheme requires small CFL at the early iterations, some explicit iteration using the forward Euler method or the four stage Runge-Kutta method (RK4) by Jameson [13] should be computed to smooth out the initial flow. Multi-block structured meshes are used for HMB2, which allow an easy sharing of the calculation load for parallel cases. ICEM-HexaTM of ANSYS is used to generate the mesh.

2.1 Chimera Method

The chimera method is available in the HMB2 solver [14]. It is based on structured composite grids with hexahedral elements, consisting of independently generated, overlapping non-matching sub-domains. A hierarchical approach is employed allowing to interpolate the solution variables based on an user-specified hierarchy of sub-domains. The interpolation between composite grids depends on a localisation procedure, that includes a localisation pre-processing and a chimera search which aim to minimise the number of searches due to potential mesh overlap. Three interpolation methods are available to control the interpolation for chimera localisation, zero order single-neighbour, inverse distance, and variable-distribution reconstruction-based interpolation. For this study, a zero order single-neighbour was used.

2.2 Actuator Disk

An uniform actuator disk was employed to assess the capability of this approach. It models the thrust force generated by the ADYN (Advanced European Tiltrotor Dynamics and Noise) [15] blades using a pressure jump on an infinitesimally thin disk. The pressure jump along the uniform actuator disk is given by:

$$(2) \quad \Delta P^* = \frac{T}{\rho_\infty V_\infty^2 S} = \frac{\rho_\infty V_{tip}^2 S C_T}{\rho_\infty V_\infty^2 S} = \frac{C_T}{\mu^2}$$

S being the rotor disk area, C_T the thrust rotor defined as $\frac{T}{\rho_\infty V_{tip}^2 S}$, and μ the rotor advance ratio.

Figure 1 presents different views of the ERICA tiltrotor, showing the relative position of the actuator disk. Note that the actuator disk was embedded in the nacelle mesh.

3 ERICA GEOMETRY AND MESH GENERATION

In this study, the chimera method was employed to ease the generation of the different multi-block grids. Self-contained component grids for the fuselage and nacelle-tiltable wing were built, while four ADYN blades were embedded in the nacelle component. A Cartesian mesh was used as the background to capture the convection of the tip vortices generated by the blades.

3.1 ERICA Mesh Generation

Table 1 compares the mesh sizes used for CFD computations with the NICETRIP project partners. The data correspond to a half aeroplane configuration.

Figure 2 (a) shows an overview of the nacelle surface mesh. According to the experimental setup [2, 3], the engine inlet of the nacelle was treated as solid. A C topology was chosen around the leading edge of the connection with the tiltable wing. For the nose of the spinner and rear part of the nacelle surface, an O topology was used.

The details of the multi-block topology of the nacelle are given in Figure 2 (b). The mesh has 30.3 millions of nodes distributed along 1770 blocks (see Table 1). Due to the fact that the four ADYN blades were embedded in the nacelle component, refinement of the nacelle mesh at the level of the rotor was required, to ensure successful interpolation between the chimera mesh components. For this configuration, the tiltable wing was not tilted with respect to the nacelle and was embedded in the nacelle mesh.

Figure 3 shows a view of the body-fitted mesh around the fuselage. An O multi-block topology was built at the front and rear parts of the fuselage, whereas a C-H multi-block topology was generated around the wing and the horizontal stabiliser.

A complete view of the multi-block topologies of the ERICA fuselage is shown in Figure 4. The fuselage mesh contains 9.9 millions of nodes along 1206 blocks (see Table 1). 290 points were used around the wind and 138 around the tail plane. The distribution of points normal to the wing and fuselage follow an exponential law with the first point located at 4×10^{-6} of the reference length.

Figure 5 shows the multi-block overset arrangement of the different grid components. Farfield and symmetry boundary conditions were applied at the

background level (Blue lines). Chimera boundaries were applied at the nacelle, blades, and fuselage levels. Note that only half of the aircraft was simulated, applying symmetry boundary conditions at the mid-plane.

4 CFD RESULTS

This section shows the CFD results for the low speed and high angle of attack aeroplane mode configuration test (case AC1). The freestream Mach number was set to 0.168. Table 2 lists the test conditions for the AC1 case. This case was selected since most NICETRIP project partners have already presented results for [16].

The first part of the results presents the distribution of the surface pressure coefficient on the fuselage, nacelle, fixed wing, and tiltable wing of the ERICA. The effect of the tunnel support on the surface pressure coefficient is also assessed. Next, visualisation of the ERICA's wake is performed using the Q -criterion. Finally, lift and drag coefficients for each component are shown, which reveals the 4/rev. blade passing effect.

4.1 Results and Discussion

The distributions of the surface pressure coefficients at eight cross sections are shown in Figure 6. They correspond to the top fuselage centre-line ($y=0$ mm), central wing section ($y=280, 490, 700,$ and 805 mm), and outer wing section ($y=855, 955,$ and 1117 mm).

Regarding the surface pressure coefficient at the centre-line of the fuselage (see Figure 7 (a)), a large zone of recirculation is seen by both sets of experiments. The HMB2 predictions over-estimate the suction peak and do not capture the region of recirculation. This can be due to the use of symmetry conditions, the employed turbulence model, and wind tunnel effects. On the other hand, the CFD results at the front part of the fuselage are in close agreement with the experimental data.

The surface pressure coefficients on the inner part of the fixed wing, at the middle of the fixed wing section, and at the middle of the tiltable section are presented in Figures 7 (b)-(h). The results with the uniform actuator disk produce adequate estimates of the wing loads. The HMB2 predictions are in good agreement with the experimental data of DNW-LLF, which shows higher wing loads than the

S1MA.

An assessment of the surface pressure coefficient on the ERICA's nacelle is given in Figure 8. Four sections were extracted corresponding to centre-line ($y=1500$ mm), bottom centre-line ($y=1500$ mm), central section ($x=1560$ mm), and rear section ($x=1860$ mm) (see Figure 8 (c)). Despite the scatter of the experimental data presented at the top and bottom centre-line of the nacelle (Figure 8 (a), (b)), the HMB2 predictions capture the nacelle loads. A slight effect of the use of the uniform actuator disk is found in these regions. Figure 8 shows the C_p at central and rear cross sections. Comparisons with the experimental data reveal the good agreement when the propellers are fully resolved (see Figure 8 (e)).

The distributions of the surface pressure coefficient at eight cross sections on the nose, central, sponson, and rear part of the ERICA fuselage are given in Figure 9. A good agreement with both experimental data is obtained for all sections.

Figure 10 (a) shows an overview of the surface pressure coefficient at the bottom part of the ERICA fuselage. Note that the tunnel support has not been modelled. The effect of the support configuration on the surface pressure coefficient at the bottom fuselage centre-line is shown in Figure 10 (b). The model of the DNW-LLF was supported via a ventral sting at the rear part of the fuselage, whereas a straight sting was set-up in the ONERA model. Both supports introduce unsteadiness in the total fuselage loads. The surface pressure coefficient is well predicted by HMB2 if compared with the experimental data of ONERA, where the support is straight. The stagnation point and the suction peak are in close agreement with the experimental data, meanwhile the pressure plateau is not well predicted.

Visualisation of the flow-field of the ERICA tiltrotor using the Q -criterion [17] coloured by Mach number is given in Figure 11. The wake behind the rotor disk is preserved for more than one rotor diameter downstream and is not captured well by the one for actuator disk model.

Lift and drag coefficients on the tiltable wing, nacelle, and fuselage with the fixed wing as functions of the blade azimuth are analysed for the ERICA tiltrotor including the rotor. The average lift and drag coefficients for the complete aircraft were also compared with the experimental data.

Figure 12 (a) shows the lift and drag coefficients on the tiltable wing and reveals the 4/rev. blade pass-

ing effect.

The nacelle lift and drag coefficients, as functions of the blade azimuth, are shown in Figure 12 (b). At the tiltable wing, the same 4/rev. behaviour is found for both coefficients.

Lift and drag coefficients of the fuselage with the fixed wing are presented in Figure 12 (c). A 4/rev. signal behaviour due to the blade passage is only seen in the drag coefficient. Finally, the coefficient of the complete ERICA tiltrotor and drag coefficient of the nacelle, tiltable wing, fixed wing, and fuselage are compared with the experimental data [3]. Table 3 lists the contribution of each component to the total average lift and drag.

5 CONCLUSIONS AND FUTURE WORK

CFD results for the NICETRIP tiltrotor configuration are presented in this paper aiming to establish the fidelity of the CFD method. The results agree well with the test data for the surface pressure coefficient on the fuselage and wing. The lack of flow separation at the aft fuselage needs more attention. This could be an effect of the symmetry used for the CFD or an effect of turbulence modelling. The effect of the model support on the C_p of the lower surface is also investigated and the straight mounted case was found to be less intrusive. The results of the CFD with an uniform actuator disk model also produced adequate estimates of the wing loads.

Computations for other test cases including hover and transition configuration are also underway.

6 ACKNOWLEDGMENTS

The use of the cluster Chadwick of the University of Liverpool is gratefully acknowledged. Part of this work is funded under the HiperTilt Project of the UK Technology Strategy Board (TSB) and AugustaWestland (AW). The authors would like to acknowledge the use of the NICETRIP experimental data and model geometry.

7 REFERENCES

- [1] "NICETRIP - Novel Innovative Competitive Effective Tilt Rotor Integrated Project: NICETRIP website," <http://www.nicetrip.onera.fr>, last visited date: 02/07/2015.
- [2] Philipsen, I. and Heinrich, S., "TEST REPORT ON MEASUREMENTS ON THE NICETRIP LARGE-SCALE POWERED MODEL IN DNW-LLF," Project number 2410.1338, DNW-LLF, Marknesse, The Netherlands, Aug. 2013.
- [3] Lebrun, F., "NICETRIP test - ERICA 1/5th scale powered model in the test section no.2 - $45m^2$ of S1MA wind tunnel," Test Report Number PV 1/17648 DSMA, ONERA, Châtillon Cedex, France, June 2014.
- [4] Lawson, S. J., Steijl, R., Woodgate, M., and Barakos, G. N., "High performance computing for challenging problems in computational fluid dynamics," *Progress in Aerospace Sciences*, Vol. 52, July 2012, pp. 19–29, doi:10.1016/j.paerosci.2012.03.004.
- [5] Steijl, R. and Barakos, G. N., "Sliding mesh algorithm for CFD analysis of helicopter rotor-fuselage aerodynamics," *International Journal for Numerical Methods in Fluids*, Vol. 58, No. 5, Oct. 2008, pp. 527–549, doi:10.1002/d.1757.
- [6] Steijl, R., Barakos, G. N., and Badcock, K., "A framework for CFD analysis of helicopter rotors in hover and forward flight," *International Journal for Numerical Methods in Fluids*, Vol. 51, No. 8, July 2006, pp. 819–847, doi:10.1002/d.1086.
- [7] Barakos, G., Steijl, R., Badcock, K., and Brocklehurst, A., "Development of CFD Capability for Full Helicopter Engineering Analysis," *Proceedings of the Thirty-First European Rotorcraft Forum*, ERF, Florence, Italy, 2005.
- [8] Hirt, C. W., Amsten, A. A., and Cook, J. L., "An Arbitrary Lagrangian-Eulerian Computing Method for All Flow Speeds," *Journal of Computational Physics*, Vol. 14, No. 3, March 1974, pp. 227–253.
- [9] Osher, S. and Chakravarthy, S., "Upwind schemes and boundary conditions with applications to Euler equations in general geometries," *Journal of Computational Physics*, Vol. 50, No. 3, June 1983, pp. 447–481, doi:10.1016/0021-9991(83)90106-7.
- [10] van Leer, B., "Towards the ultimate conservative difference scheme. V.A second-order sequel to Godunov's Method," *Journal of Computational Physics*, Vol. 32, No. 1, July 1979, pp. 101–136, doi:10.1016/0021-9991(79)90145-1.
- [11] van Albada, G. D., van Leer, B., and Roberts, W. W., "A Comparative Study of Computational Methods in Cosmic Gas Dynamics," *Astronomy and Astrophysics*, Vol. 108, No. 1, April 1982, pp. 76–84.
- [12] Axelsson, O., "Iterative Solution Methods," Cambridge University Press, Cambridge, 1996, pp. 1–654.
- [13] Jameson, A., Schmidt, W., and Turkel, E., "Numerical Solutions of Euler Equations by Finite-Volume Methods Using Runge-Kutta Time-Stepping Schemes," *AIAA Paper 81-1259*, June 1981.
- [14] Jarkowski, M., Woodgate, M., Barakos, G. N., and Rokicki, J., "Towards consistent hybrid overset mesh methods for rotorcraft CFD," *International Journal for Numerical Methods in Fluids*, Vol. 74, No. 8, 2014, pp. 543–576, doi:10.1002/flid.3861.
- [15] Crozier, P., "Tests on ADYN and Tilt Aero Rotor Blades Performed in S1 Modane Wind Tunnel," Test Report Number PV 1/10971 DAAP/DSMA, ONERA, Châtillon Cedex, France, Feb. 2009.
- [16] Decours, J., Beaumier, P., Khier, W., Kneisch, T., Valentini, M., and Vigeveno, L., "Experimental Validation of Tilt-Rotor Aerodynamic Predictions," *Proceeding of the Fortieth European Rotorcraft Forum*, ERF, Southampton, UK, 2014.
- [17] Jeong, J. and Hussain, F., "On the identification of a vortex," *Journal of Fluid Mechanics*, Vol. 285, Feb. 1995, pp. 69–94, doi:10.1017/S0022112095000462.

- [18] Kroll, N., Eisfeld, B., and Bleecke, H., "The Navier-Stokes Code FLOWer," *Notes on Numerical Fluid Mechanics, Vieweg, Braunschweig*, Vol. 71, 1999, pp. 58–71.
- [19] Cambier, L., Heib, S., and Plot, S., "The Onera elsA CFD software: input from research and feedback from industry," *Mechanics&Industry - Cambridge Journals*, Vol. 14, No. 3, 2013, pp. 159–174, doi:10.1051/meca/2013056.
- [20] Biava, M., *RANS computations of rotor/fuselage unsteady interactional aerodynamics*, Ph.D. thesis, Dipartimento di Ingegneria Aerospaziale, Politecnico di Milano, Milano, Italy, 2007.
- [21] Wilcox, D., "Reassessment of the scale-determining equation for advanced turbulence models," *AIAA journal*, Vol. 26, No. 11, 1988, pp. 1299–1310, doi:10.2514/3.10041.

Components	UoL [4, 5, 6, 7]	AHD [18]	ONERA [19]	Polimi [20]	DLR [18]
Fuselage and fixed wing	9.9	18.6	5.8	5.6	36.7
Tiltable wing	-	1.7	2	2	0.7
Nacelle	30.3	5.7	3.8	3.8	10.4
Rotor blades (x4)	11.4	-	4	4	5.4
Actuator disc	-	0.4	-	-	-
Model support	-	2.3	0.8	0.8	0.3
Wind tunnel	4.6	10.8	9.8	9.8	0.5
Total	56.2	39.5	26.2	26	53.9

Table 1: ERICA model component mesh sizes, given as number of nodes $\times 10^6$.

Test Conditions	Value
M_∞	0.168
M_{tip}	0.47
Re_∞	1.7×10^6
AoA	10.02°
RPM blade rotor	2130
Blade collective angle ($\theta_{75\%}$)	27.36°

Table 2: Test conditions for the ERICA tiltrotor in aeroplane mode configuration [2, 3].

Component	HMB2		Wind tunnel	
	C_L	C_D	C_L	C_D
Tiltable wing	0.244	0.012	-	-
Nacelle	0.039	0.017	-	-
Fuselage	0.432	0.041	-	-
Rotor	0.073	-	-	0.053
Total	0.789	0.071	0.683	0.053

Table 3: Comparison of the average lift and drag coefficient through one rotor revolution, showing the contribution of each component. $M_\infty = 0.168$, $Re_\infty = 1.7 \times 10^6$, AoA= 10.02° degrees. The surface used as a reference was $S_{ref}=1.4 \text{ m}^2$.

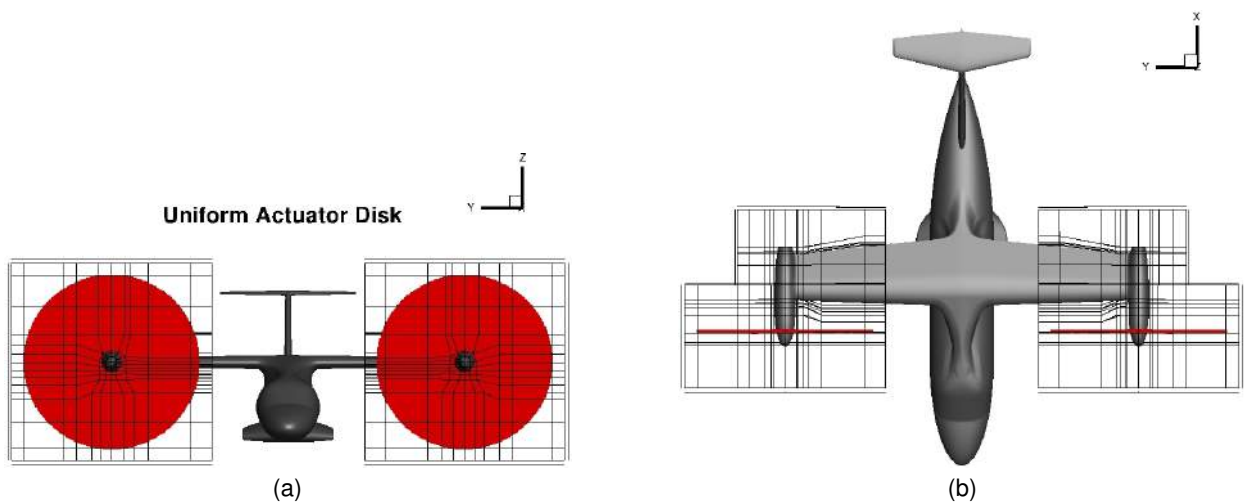


Figure 1: (a) Front view and (b) top view of the ERICA tiltrotor, showing the position of the uniform actuator disk.

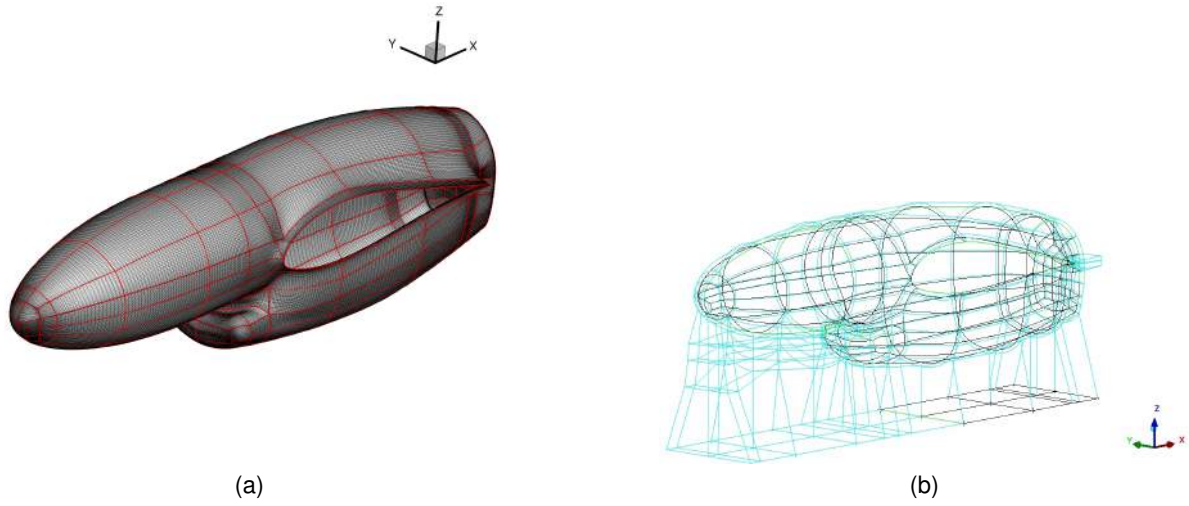


Figure 2: (a) Surface mesh distribution and (b) multi-block topology of the ERICA's nacelle.

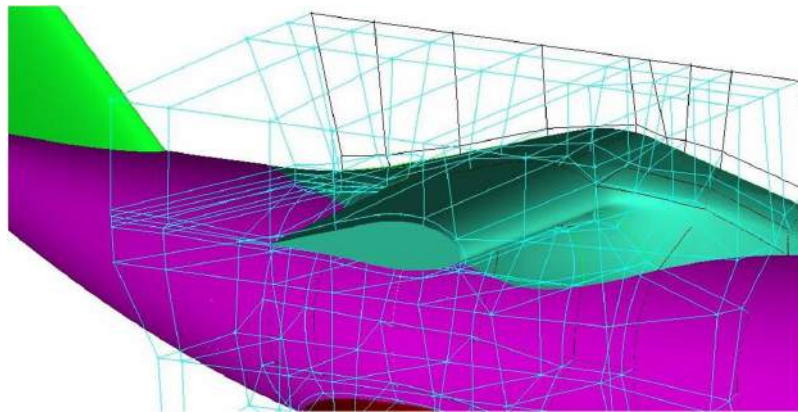


Figure 3: Multi-block topology around the fuselage: close view at the fixed wing.

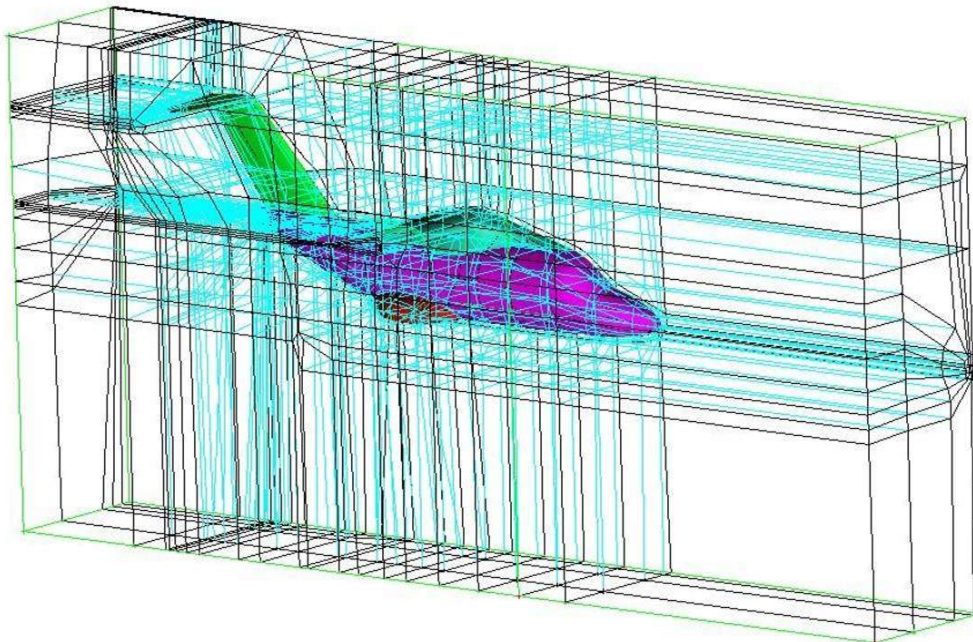


Figure 4: Overview of the multi-block topology of the ERICA's fuselage. 9.9 millions of nodes and 1206 blocks (see Table 1).

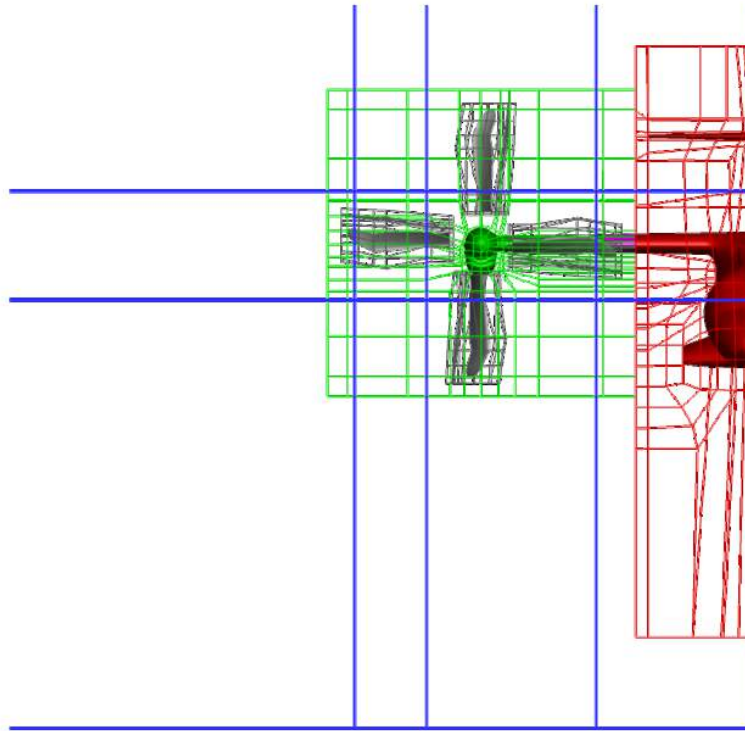


Figure 5: Details of the multi-block overset arrangement of the ERICA tiltrotor in aeroplane mode configuration. Blue line: Background component, Red line: Fuselage component, Green line: Nacelle component and Grey line: Blade component.

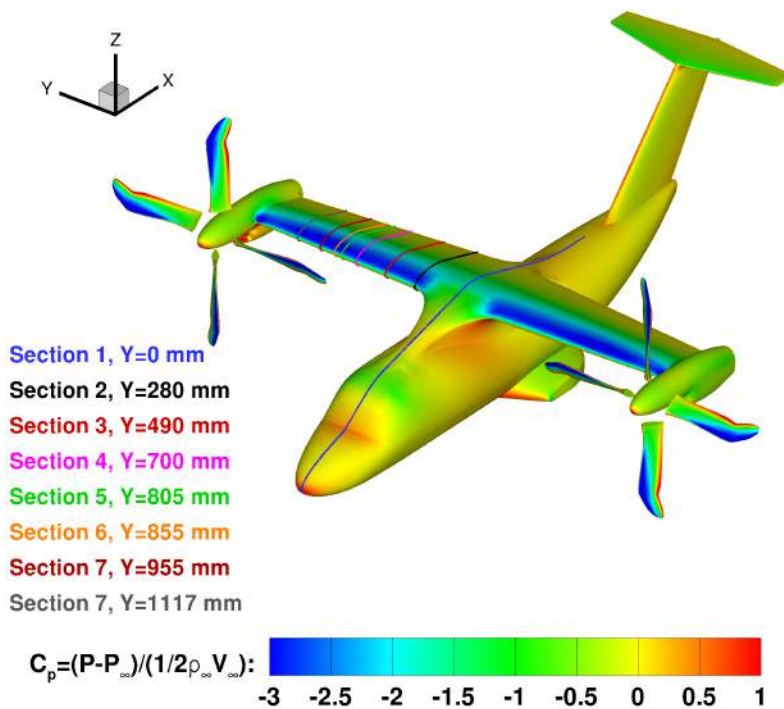
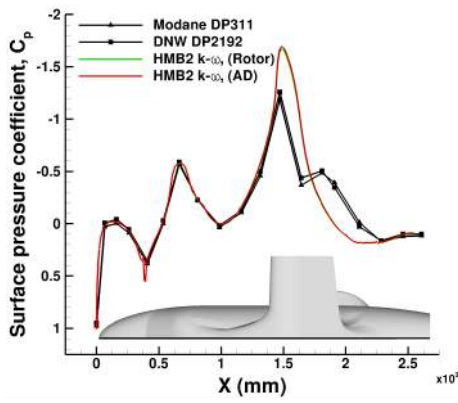
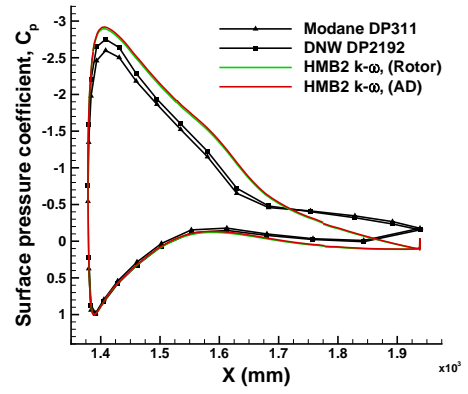


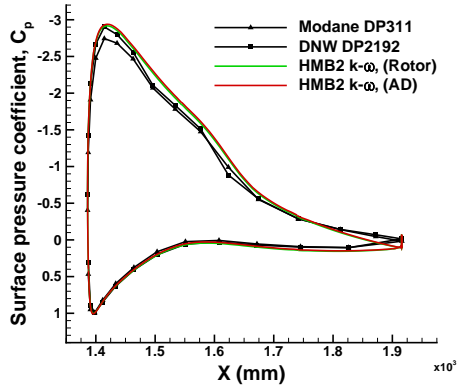
Figure 6: Overview of the surface pressure coefficient of the ERICA tiltrotor, showing the location of the eight cross-sections selected for comparison with experimental data. $M_\infty=0.168$, $Re_\infty=1.7 \times 10^6$, and $AoA=10.02^\circ$. Wilcox's $k-\omega$ [21] model was used.



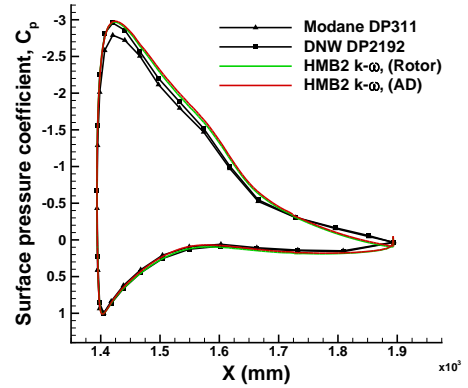
(a) Top fuselage centre-line $y=0$ mm.



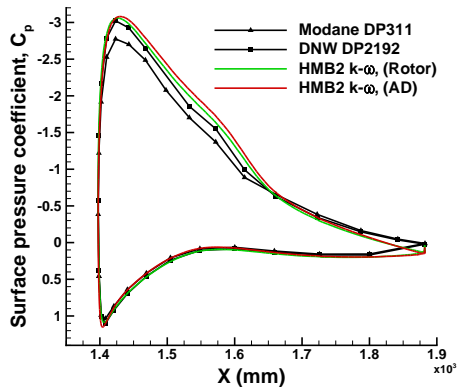
(b) Central wing section $y=280$ mm.



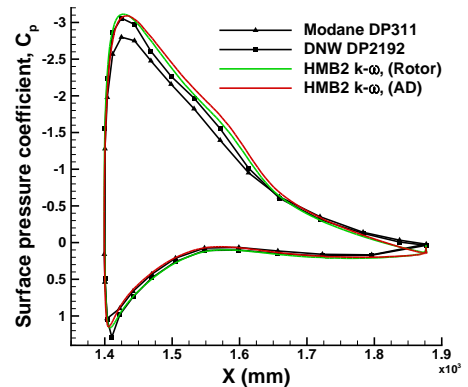
(c) Central wing section $y=490$ mm.



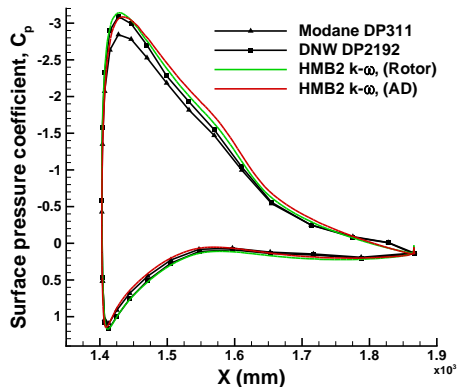
(d) Central wing section $y=700$ mm.



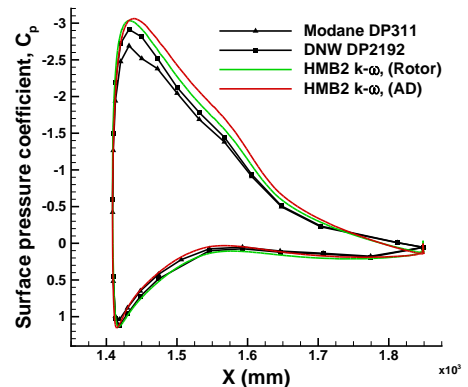
(e) Central wing section $y=805$ mm.



(f) Outer wing section $y=855$ mm.

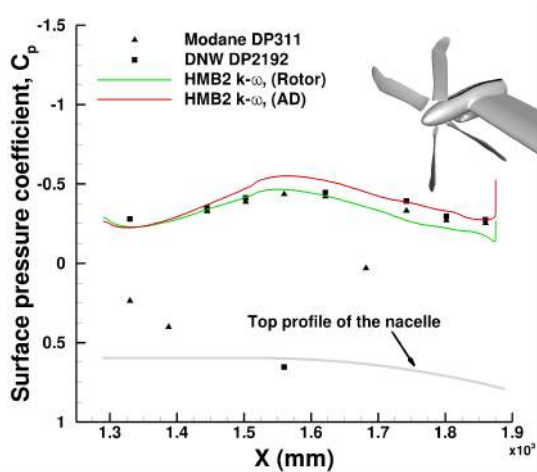


(g) Outer wing section $y=955$ mm.

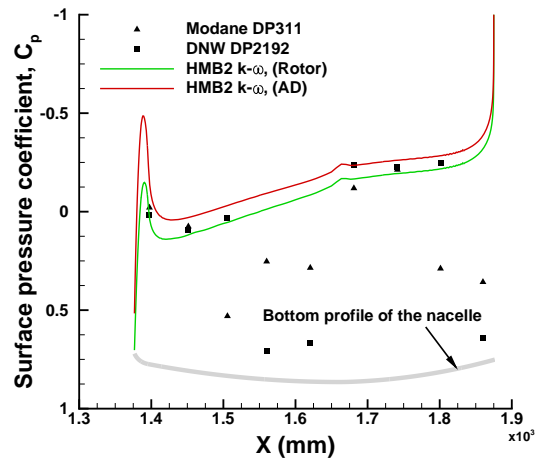


(h) Outer wing section $y=1117$ mm.

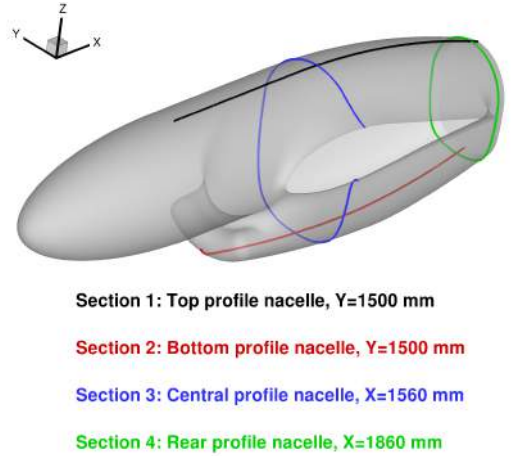
Figure 7: Distributions of surface pressure coefficient at eight cross sections on the fuselage, tiltable, and fixed wing. $M_\infty=0.168$, $Re_\infty=1.7 \times 10^6$, and $AoA=10.02^\circ$. Wilcox's $k-\omega$ [21] model was used.



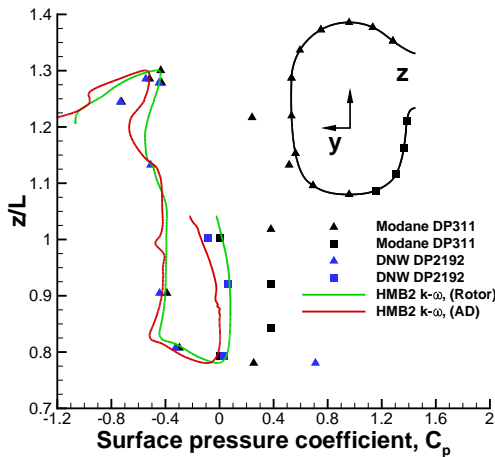
(a) Top centre-line $y=1500$ mm.



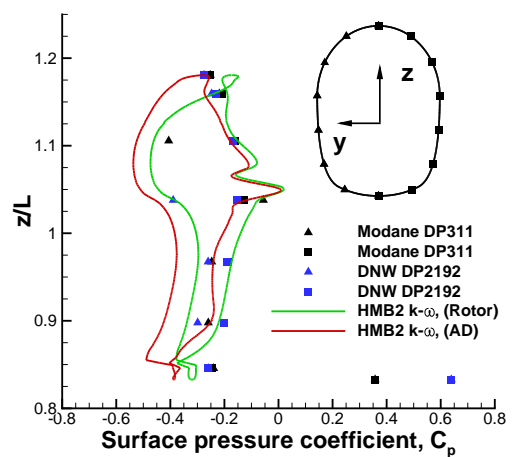
(b) Bottom centre-line $y=1500$ mm.



(c) Overview of the nacelle.

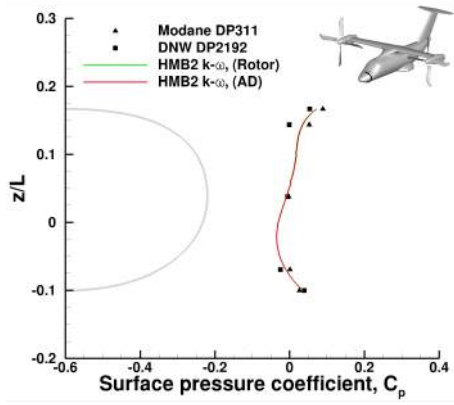


(d) Central section $x=1560$ mm.

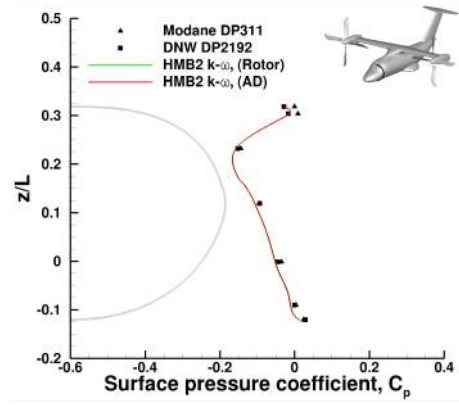


(e) Rear section $x=1860$ mm.

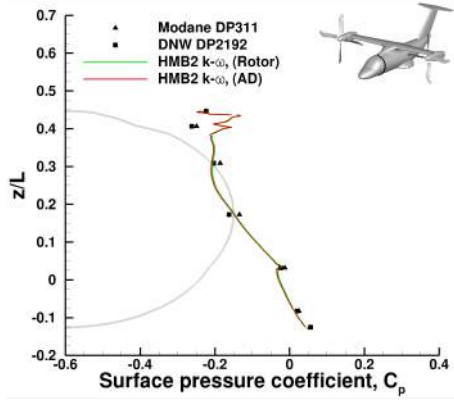
Figure 8: Distributions of surface pressure coefficient at the top centre-line, bottom centre-line, central section, and rear section of the nacelle. $M_\infty=0.168$, $Re_\infty=1.7 \times 10^6$, and $AoA=10.02^\circ$. Wilcox's $k-\omega$ [21] model was used.



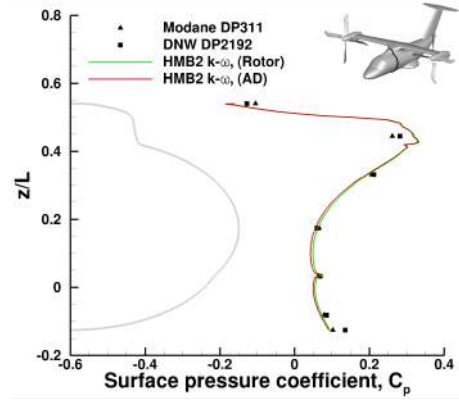
(a) Nose fuselage section $x=500$ mm.



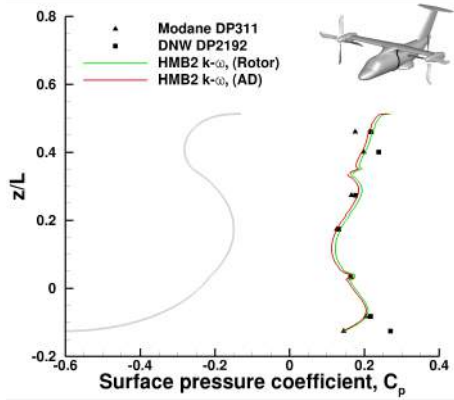
(b) Nose fuselage section $x=775$ mm.



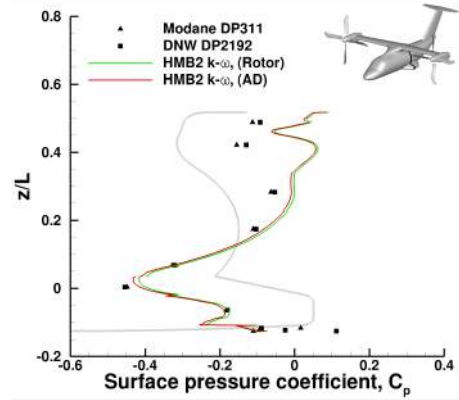
(c) Nose fuselage section $x=1050$ mm.



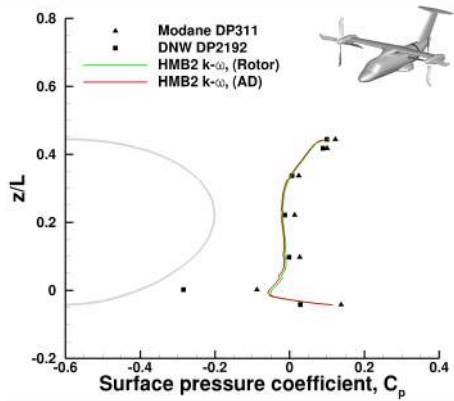
(d) Central fuselage section $x=1403$ mm.



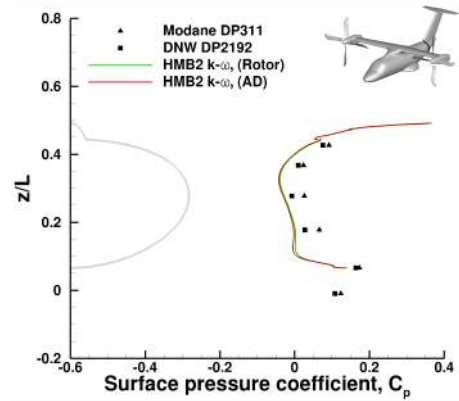
(e) Central fuselage section $x=1710$ mm.



(f) Sponson section $x=2050$ mm.

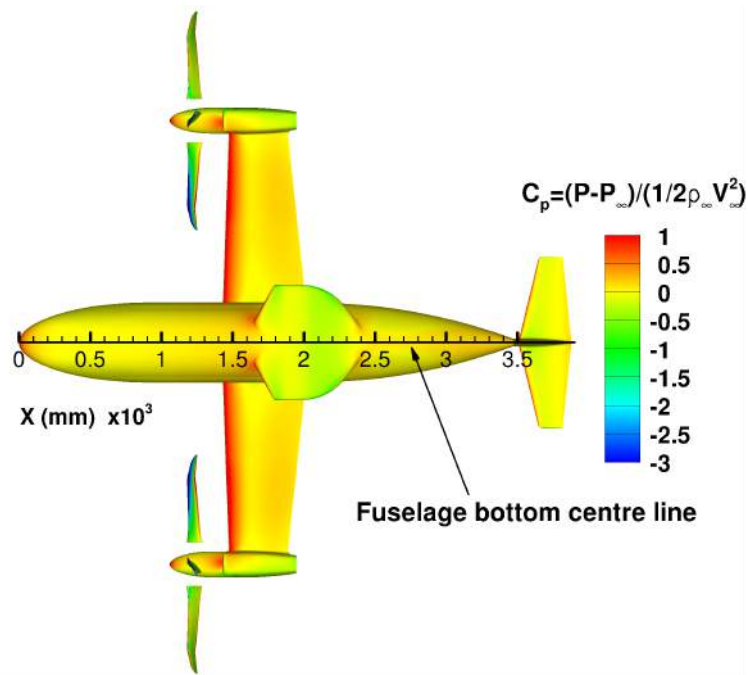


(g) Rear fuselage section $x=2700$ mm.

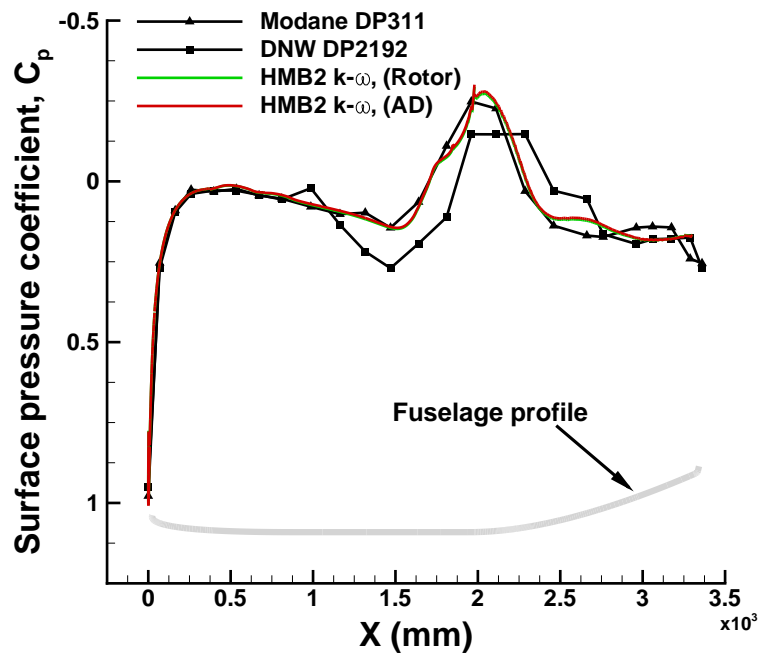


(h) Rear fuselage section $x=3000$ mm.

Figure 9: Distributions of surface pressure coefficient at eight cross sections on the nose, central, sponson, and rear part of the ERICA fuselage. $M_\infty=0.168$, $Re_\infty=1.7 \times 10^6$, and $AoA=10.02$ degrees. Wilcox's $k-\omega$ [21] model was used.



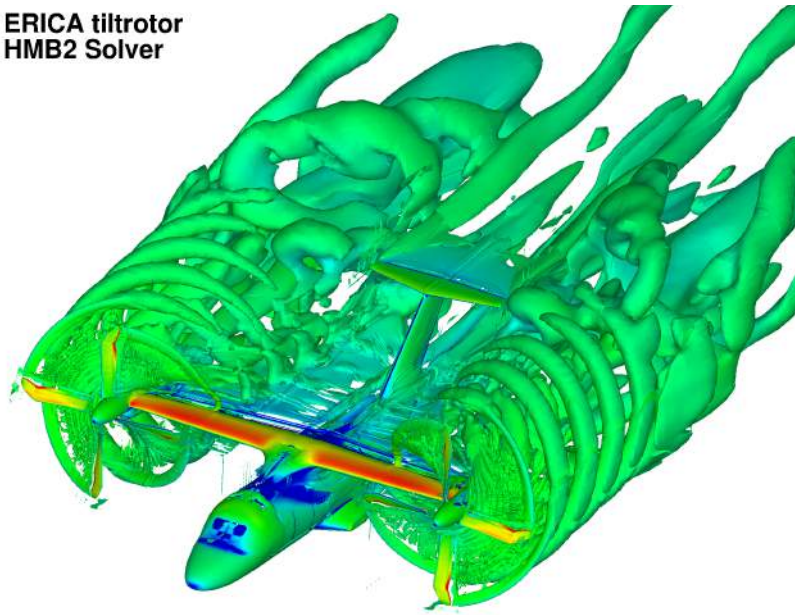
(a)



(b)

Figure 10: (a) Overview of the surface pressure coefficient at the bottom part of the ERICA tiltrotor in aeroplane mode and (b) Effect of the model support on the surface pressure coefficient. $M_\infty=0.168$, $Re_\infty=1.7 \times 10^6$, and $AoA=10.02$ degrees. Wilcox's $k-\omega$ [21] model was used.

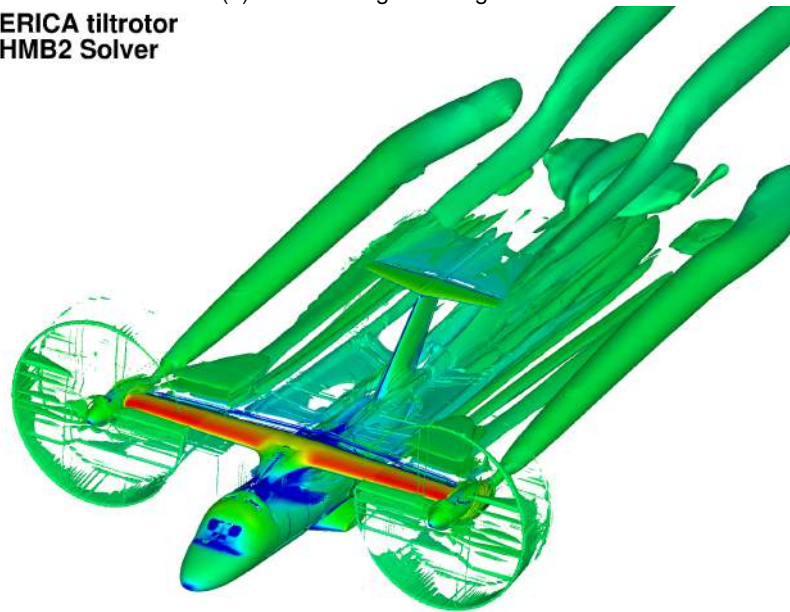
ERICA tiltrotor
HMB2 Solver



Mach Number: 0.05 0.1 0.15 0.2 0.25 0.3 0.35

(a) Azimuth angle= 0 degrees.

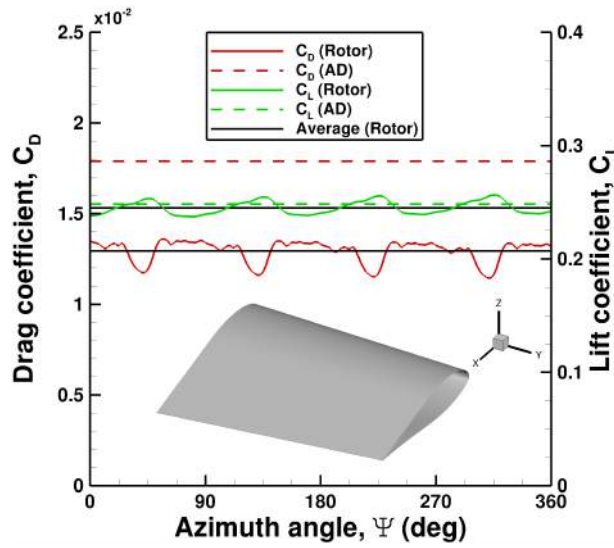
ERICA tiltrotor
HMB2 Solver



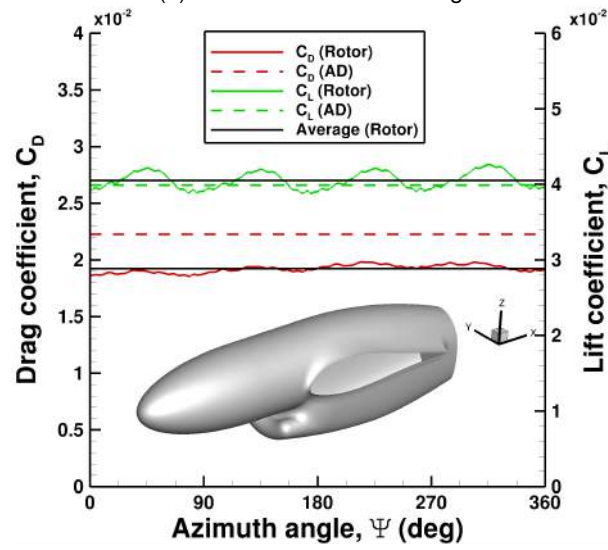
Mach Number: 0.05 0.1 0.15 0.2 0.25 0.3 0.35

(b) Actuator disk.

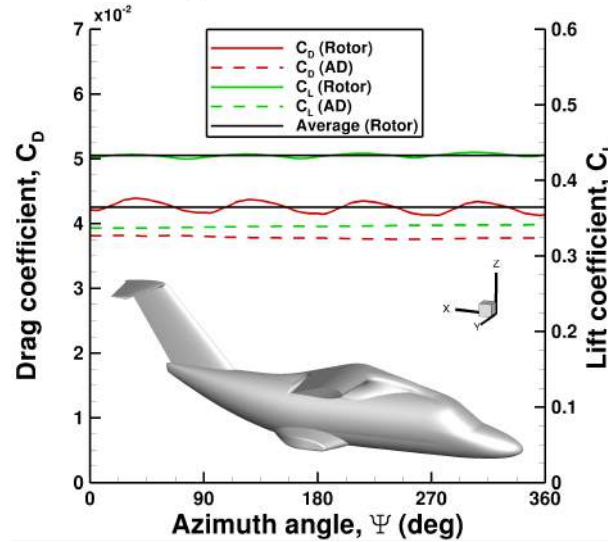
Figure 11: Visualisation of the ERICA tiltrotor in aeroplane mode using Q -criterion and coloured by contour of Mach number. Figure (a) corresponds to the numerical simulation performed with the propellers-on at 0 degrees of azimuth angles, whereas Figure (b) corresponds to the uniform actuator disk. $M_\infty=0.168$, $Re_\infty=1.7\times 10^6$, and $AoA=10.02$ degrees. Wilcox's $k-\omega$ [21] model was used.



(a) Loads on the tiltable wing.



(b) Loads on the nacelle.



(c) Loads on the fuselage and fixed wing.

Figure 12: History of the lift and drag coefficients in the (a) tiltable wing, (b) nacelle, and (c) fuselage and fixed wing of the ERICA tiltrotor in aeroplane mode. $M_\infty=0.168$, $Re_\infty=1.7 \times 10^6$, and $AoA=10.02$ degrees. Wilcox's $k-\omega$ [21] model was used. The surface used as a reference was $S_{ref}=1.4 \text{ m}^2$.